PAPER

Multi-step hydration/dehydration mechanisms of rhombohedral $Y_2(SO_4)_3$: a candidate material for low-temperature thermochemical heat storage†

Kunihiko Shizume, [ID] * Naoyuki Hatada,* Shoko Yasui and Tetsuya Uda*

To evaluate rhombohedral $Y_2(SO_4)_3$ as a new potential material for low-temperature thermochemical energy storage, its thermal behavior, phase changes, and hydration/dehydration reaction mechanisms are investigated. Rhombohedral $Y_2(SO_4)_3$ exhibits reversible hydration/dehydration below 130 °C with relatively small thermal hysteresis (less than 50 °C). The reactions proceed *via* two reaction steps in approximately 0.02 atm of water vapor pressure, *i.e.* "high-temperature reaction" at 80–130 °C and "low-temperature reaction" at 30–100 °C. The high-temperature reaction proceeds by water insertion into the rhombohedral $Y_2(SO_4)_3$ host structure to form rhombohedral $Y_2(SO_4)_3 \cdot xH_2O$ ($x = \sim1$). For the low-temperature reaction, rhombohedral $Y_2(SO_4)_3 \cdot xH_2O$ accommodates additional water molecules ($x > 1$) and is eventually hydrated to $Y_2(SO_4)_3 \cdot 8H_2O$ (monoclinic) with changes in the host structure. At a water vapor pressure above 0.08 atm, intermediate $Y_2(SO_4)_3 \cdot 3H_2O$ appears. A phase stability diagram of the hydrates is constructed and the potential usage of $Y_2(SO_4)_3$ for thermal energy upgrades is assessed. The high-temperature reaction may act similarly to an existing candidate, $CaSO_4 \cdot 0.5H_2O$, in terms of reaction temperature and water vapor pressure. Additionally, the hydration of rhombohedral $Y_2(SO_4)_3 \cdot xH_2O$ to $Y_2(SO_4)_3 \cdot 3H_2O$ should exhibit a larger heat storage capacity. With respect to the reaction kinetics, the initial dehydration of $Y_2(SO_4)_3 \cdot 8H_2O$ to rhombohedral $Y_2(SO_4)_3$ introduces a microstructure with pores on the micron order, which might enhance the reaction rate.

1. Introduction

Thermal energy storage based on chemical reactions (TCHS: thermochemical heat storage) is a prospective technology for the reduction of fossil-fuel consumption by storing waste heat.[1,2] One of the expected roles of TCHS is storing and utilizing heat below 250 °C, where abundant low-grade waste heat and solar energy might be available. For widespread application, a critical challenge is to identify appropriate reversible dehydration/hydration reaction systems satisfying following criteria: suitable reaction temperature, enabling high heat storage capacity, fast enough reaction rate and heat output rate, long-term stability of thermophysical and mechanical properties including, for example, no liquefaction due to melting or deliquescence, non-toxicity of materials themselves and reaction products, the low cost of materials, *etc.*[3] Solid–gas reactions using water vapor as a reactive gas (dehydration/hydration reactions) are favorable because water is safe and easily stored *via* condensation. To date, various salt hydrates, whose dehydration/hydration reactions can be operated below

250 °C, have been proposed, for example, $MgSO_4 \cdot nH_2O$ ($n = 0$–7),[4–6] $CaCl_2 \cdot nH_2O$ ($n = 0$–6),[7] $LiOH \cdot H_2O$,[8–10] $Na_2S \cdot 5H_2O$,[11,12] and $CaSO_4 \cdot 0.5H_2O$.[13,14] However, these salt hydrates suffer from some undesirable behaviors related to hydration kinetics and cycle performance.‡ Despite numerous efforts related to the modification of material properties such as developing composite materials based on these salt hydrates, no materials have been widely used yet.

Recently, we reported the dehydration/hydration of β-$La_2(SO_4)_3 \cdot H_2O$ as a new candidate reaction for TCHS below 250 °C.[15–17] The reactions proceed by insertion/deinsertion of the H_2O guest molecules into β-$La_2(SO_4)_3$ host lattices,§ which

Department of Materials Science and Engineering, Kyoto University, Yoshida Honmachi, Sakyo-ku, Kyoto, 606-8501, Japan. E-mail: shizume.kunihiko.26z@st. kyoto-u.ac.jp; hatada.naoyuki.8u@kyoto-u.ac.jp; uda.tetsuya.5e@kyoto-u.ac.jp

† Electronic supplementary information (ESI) available. See DOI: 10.1039/d0ra02566f

‡ The major problems of these salt hydrates are described below. $MgSO_4 \cdot nH_2O$ ($n = 0$–7): shape instability due to the melting of the salt which occurs during dehydration of $MgSO_4 \cdot 7H_2O$ to $MgSO_4 \cdot 6H_2O$.[5] In addition, the fine powder rapidly forms a skin of the hydrated salt on the surface when it reacts with humid air, which decreases the reaction rate.[6] $CaCl_2 \cdot nH_2O$ ($n = 0$–6): agglomeration of the salt due to partial melting of the salt during the dehydration or a partial formation of a solution of the salt attributed to the hygroscopicity during rehydration, which decreases the reaction rate.[7] $LiOH \cdot H_2O$: the low hydration reaction rate of pure LiOH which limits the performance of low-temperature TCHS systems.[9,10] $Na_2S \cdot 5H_2O$: generation of toxic by-product H_2S gas by contacting with water.[12] $CaSO_4 \cdot 0.5H_2O$: degradation due to phase transformation from $CaSO_4$ (III) to the low-hydration-reactive phase $CaSO_4$ (II) during repetitive dehydration/hydration reaction.[13,14]

§ $CaSO_4 \cdot 0.5H_2O$ is also known to dehydrate and rehydrate by deinsertion and insertion of H_2O guest molecules into the sulfate host lattice.[18]

leads the rapid and reversible dehydration/hydration reaction even at low-temperature below 250 °C. Furthermore, β-La$_2$(SO$_4$)$_3$ is non-toxic and does not show melting and deliquescence. However, the heat storage capacity is insufficient due to the small changes in the hydration water content (β-La$_2$(SO$_4$)$_3 \cdot$H$_2$O: 3.2 mass% anhydrous basis). There is still a need to find other materials.

In this study, we focused on Y$_2$(SO$_4$)$_3$ as a new candidate material for the low-temperature TCHS system. Y$_2$(SO$_4$)$_3$ is another trivalent-rare-earth sulfate with a chemical formula analogous to that of β-La$_2$(SO$_4$)$_3$ but it has a crystal structure belonging to the rhombohedral system (space group: No. 148).[19] Due to the differences of rare-earth elements and crystal structures, the hydration/dehydration behavior of rhombohedral Y$_2$(SO$_4$)$_3$ should differ from that of β-La$_2$(SO$_4$)$_3$ (monoclinic system, space group: 15). Thus it is worthwhile to investigate if rhombohedral Y$_2$(SO$_4$)$_3$ shows favorable hydration/dehydration behaviors. See ESI-1† for their crystal structures. Though there are a few studies associated with the phase changes, reaction temperature, and enthalpy changes on dehydration of Y$_2$(SO$_4$)$_3 \cdot$8H$_2$O,[20–22] the backward hydration reaction behaviors have not been reported. In addition, Y$_2$O$_3$, the raw material of Y$_2$(SO$_4$)$_3$, is oversupplied, so the cost is not expensive at this time, 3 USD kg^{-1} in 2018.[23] Therefore, Y$_2$(SO$_4$)$_3$ might be a low-cost candidate for TCHS.

In this work, thermogravimetry (TG) studies of the hydration/dehydration reaction were conducted. High-temperature X-ray diffraction (XRD) investigated the crystal structure changes in the dehydration reaction. Then, we systematically investigated the phases formed in the hydration process under various conditions of temperatures and water vapor pressure p_{H_2O} and discussed the available reactions for TCHS system. In addition, we examined the microstructures of Y$_2$(SO$_4$)$_3$ and Y$_2$(SO$_4$)$_3 \cdot$8H$_2$O by nitrogen gas adsorption (N$_2$ adsorption), optical microscopy, and transmission electron microscopy (TEM) because the microstructures should influence the dehydration/hydration reaction rates.[17]

2. Experimental

2.1 Materials

In this paper, a-few-hundreds-μm-large particles of Y$_2$(SO$_4$)$_3 \cdot$8H$_2$O (Strem Chemical, 99.9%) were used as the starting material for the syntheses of rhombohedral Y$_2$(SO$_4$)$_3$ by heating Y$_2$(SO$_4$)$_3 \cdot$8H$_2$O. The heating processes were either conducted at the time of thermogravimetry, high-temperature XRD and N$_2$ adsorption measurements in the respective apparatus or pre-conducted in a stand-alone furnace.

2.2 Thermogravimetry (TG)

To investigate the dehydration/hydration reaction behavior of rhombohedral Y$_2$(SO$_4$)$_3$, TG was conducted using a Rigaku Thermo plus TG 8120. Y$_2$(SO$_4$)$_3 \cdot$8H$_2$O was heated to about 400 °C, which is the temperature where dehydration to the anhydrate should be completed, and subsequently cooled to about 30 °C in the TG apparatus ("first heating–cooling cycle") under a humidified argon gas (water vapor pressure p_{H_2O} = 0.02 atm) flow. At this

point, Y$_2$(SO$_4$)$_3 \cdot x$H$_2$O was obtained as a rehydrated phase of anhydrate Y$_2$(SO$_4$)$_3$. On the subsequent "second heating–cooling cycle" between 30–160 °C, the dehydration/hydration reaction behaviors of Y$_2$(SO$_4$)$_3 \cdot x$H$_2$O were investigated. Isothermal TG measurements at various temperatures in humidified argon (p_{H_2O} = 0.023 atm) were conducted on the hydration of rhombohedral Y$_2$(SO$_4$)$_3$. For isothermal TG measurements, Y$_2$(SO$_4$)$_3 \cdot$8H$_2$O was used as the starting material and it was dehydrated to rhombohedral Y$_2$(SO$_4$)$_3$ upon heating to 320 °C in dry argon by TG. Subsequently, it was cooled to arbitrary temperatures and the isothermal hydration reaction started by switching flowing gas from dry argon to humidified argon.

In all the TG measurements, the sample material was put in a platinum cylindrical crucible with a diameter of 5 mm and a height of 5 mm and the same empty crucible was used as the reference.

2.3 X-ray diffraction (XRD)

XRD measurements were conducted on a PANalytical X'Pert-Pro MPD using Cu Kα radiation. High-temperature data collection was achieved using an Anton Paar HTK1200N high-temperature oven-chamber under humidified oxygen. For the high-temperature XRD experiments, Y$_2$(SO$_4$)$_3 \cdot$8H$_2$O (Strem Chemical, 99.9%) was heated to 300 °C to form rhombohedral Y$_2$(SO$_4$)$_3$ and subsequently, it was cooled to 50 °C to form the hydrated phase Y$_2$(SO$_4$)$_3 \cdot x$H$_2$O. The XRD patterns during dehydration of Y$_2$(SO$_4$)$_3 \cdot x$H$_2$O were collected on the second heating process from 50 °C to 150 °C. All heating/cooling processes for *in situ* XRD measurements were conducted under 0.03 atm of p_{H_2O}. Rietveld refinement analyses were performed with the help of a commercial software X'Pert HighScorePlus (PANalytical) on the *in situ* XRD patterns to identify the phase and the lattice parameters of the samples.

2.4 Isothermal hydration treatments of Y$_2$(SO$_4$)$_3$ under various temperature and p_{H_2O}

The phases formed by the hydration of Y$_2$(SO$_4$)$_3$ under arbitrary temperatures (37–84 °C) and p_{H_2O} (0.03–0.4 atm) were investigated by isothermal hydration treatments using two electric furnaces. Rhombohedral Y$_2$(SO$_4$)$_3$ was prepared by dehydration of Y$_2$(SO$_4$)$_3 \cdot$8H$_2$O at 200 °C for 1 hour in air. Rhombohedral Y$_2$(SO$_4$)$_3$ (0.1 g) was placed in an approximately 60 mL closed vessel. The vessel and a tank with water were put in separate furnaces and they were connected by the gas line across the furnaces. The vessel was maintained at a constant temperature for 3 hours while the p_{H_2O} control was performed by flowing humidified argon gas at a rate of 200 mL min^{-1} bubbled through water kept at a constant temperature. A ribbon heater was wrapped around the gas line outside the furnaces and kept over 80 °C to prevent condensation of water vapor in humidified argon gas.

The phases of the sample after the hydration treatments were identified by XRD. Fourteen batches under different conditions of temperature and p_{H_2O} were examined. Based on the results of the isothermal TG and hydration treatments, the phase stability diagram of Y$_2$(SO$_4$)$_3$ with temperature and water vapor pressure axes (T–p_{H_2O} map) was constructed.

2.5 Nitrogen gas adsorption measurements (N_2 adsorption)

The specific surface areas of the samples were evaluated by N_2 adsorption measurements at the liquid nitrogen temperature (77 K) using a BEL JAPAN BELSORP-max. $Y_2(SO_4)_3 \cdot 8H_2O$ (5.758 g) and rhombohedral $Y_2(SO_4)_3$ (1.321 g), which was prepared by heating $Y_2(SO_4)_3 \cdot 8H_2O$ at 200 °C for 1 hour in air, were placed in a Pyrex glass tube and subjected to a vacuum heating pretreatment. Afterward, N_2 adsorption measurements were conducted.

2.6 Optical microscope and TEM observations

Change in the morphology of the particles during the dehydration process of $Y_2(SO_4)_3 \cdot 8H_2O$ to rhombohedral $Y_2(SO_4)_3$ was analyzed by optical microscopy using a Nikon L150 L-150II-TI-DIC-A. $Y_2(SO_4)_3 \cdot 8H_2O$ was observed by the optical microscope as it is. Rhombohedral $Y_2(SO_4)_3$ made by heating $Y_2(SO_4)_3 \cdot 8H_2O$ at 270 °C for 2 hours in air and was observed by the optical microscope.

The microstructure inside the rhombohedral $Y_2(SO_4)_3$ particle was observed by TEM using a JEOL JEM-2100F. The rhombohedral $Y_2(SO_4)_3$ specimen for the TEM observation was cut out from the particle by a focused ion beam (FIB) using a JEOL JIB-4600F.

3. Results

3.1 Hydration/dehydration reaction behaviors of rhombohedral $Y_2(SO_4)_3$

Fig. 1 shows a TG curve of rhombohedral $Y_2(SO_4)_3$ upon cooling/heating in humidified argon. Rhombohedral $Y_2(SO_4)_3$ can hydrate/dehydrate below 130 °C with relatively small thermal hysteresis (below 50 °C). The change in the hydration number x is greater than 1 and the total mass change in the hydration
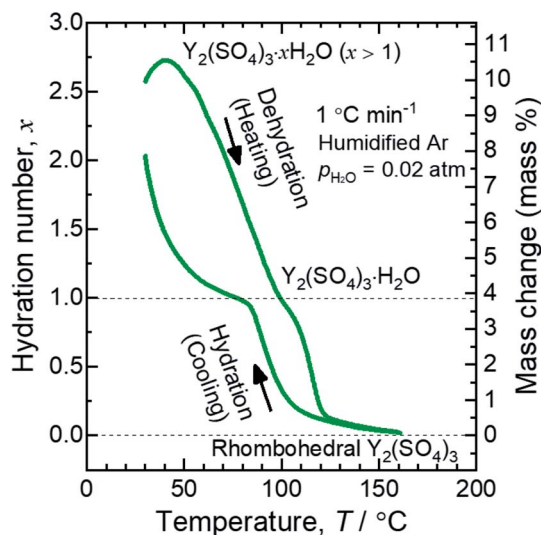
water content is larger than 10 mass% anhydrous basis. This value is larger than that of $La_2(SO_4)_3$ (3 mass%) and $CaSO_4$ (6 mass%) and a higher heat storage capacity is expected. Therefore, it may be a suitable material for the temperature range.

The TG curve (Fig. 1) suggests that the dehydration/hydration reactions proceed via two reaction steps. The temperature ranges of these two reaction steps are overlapping, preventing them from being clearly distinguished. Between 80–130 °C, apparent hydration number x varies steeply from 0 to approximately 1 ("high-temperature dehydration/hydration reaction"). Below 80 °C, $Y_2(SO_4)_3 \cdot H_2O$ forms a hydrate with a larger hydration number in the cooling process. The dehydration/hydration reaction proceeds at 30–100 °C ("low-temperature dehydration/hydration reaction"). Both the high-temperature reaction and the low-temperature reaction may be useful for TCHS system. On the other hand, the phase changes in each reaction step are not established. Rosso et al. already reported the relationship between the reaction temperatures and formed hydrate phases of $Y_2(SO_4)_3$.
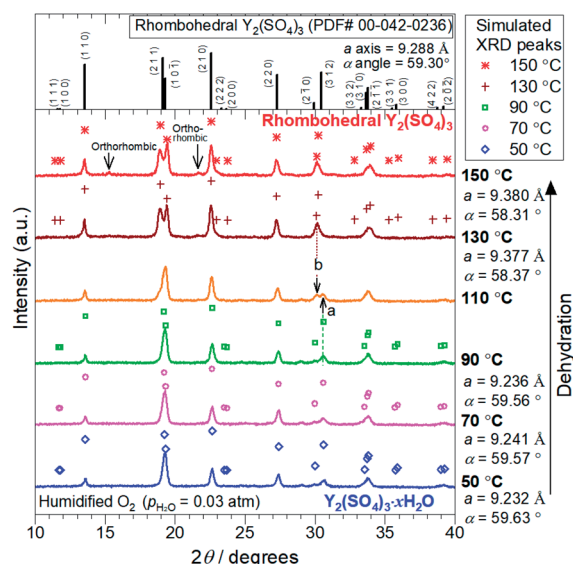
Fig. 2 High-temperature XRD patterns collected during the dehydration reaction of $Y_2(SO_4)_3 \cdot xH_2O$ to rhombohedral $Y_2(SO_4)_3$ in the heating process under humidified oxygen ($p_{H_2O} = 0.03$ atm). Topmost chart shows the reported XRD pattern of rhombohedral $Y_2(SO_4)_3$, which is cited from ICDD (PDF#00-042-0236). The other part shows the measured XRD patterns and the simulated XRD peaks at each temperature. Marks shown above XRD patterns denote simulated XRD peaks obtained by Rietveld refinement using rhombohedral $Y_2(SO_4)_3$ (PDF#00-042-0236) as the initial crystal structure. The diffraction angles of simulated XRD peaks are determined by the results of lattice parameter refinements shown on the right side of the figure below each measurement temperature. Note that the intensities of simulated XRD peaks are assumed to be the same as the reported pattern (PDF#00-042-0236). Peak a and peak b in the XRD pattern at 110 °C, indicated by black arrows, are attributed to $Y_2(SO_4)_3 \cdot xH_2O$ and rhombohedral $Y_2(SO_4)_3$ respectively. Two weak peaks, indicated as "orthorhombic", in XRD pattern at 150 °C represent the slight formation of orthorhombic $Y_2(SO_4)_3$. The peaks are identified by the reported pattern of orthorhombic $Y_2(SO_4)_3$ (ICDD, PDF#04-009-9561).

Fig. 1 TG curve of rhombohedral $Y_2(SO_4)_3$ undergoing hydration/dehydration reactions upon cooling/heating. Vertical axis in right side shows the mass changes of the sample. Vertical axis in left side shows apparent hydration number x calculated from the mass change. (Note: This data was presented at IMPRES2019.[24])

Table 1 Summary of the results of the isothermal TG measurements and the isothermal hydration (IH) treatments

| Expt. # | Temp. (°C) | p_{H_2O} (atm) | Time (h) | x^b | Detected hydrated phases[c] | | | | |
					$Y_2(SO_4)_3 \cdot 8H_2O$	$Y_2(SO_4)_3 \cdot 3H_2O$	Rhombo-hedral[d]	Unknown A	Unknown B
TG 1	27.2	0.023	3^a	6.3	Strong	—	Weak	—	—
TG 2	37.8	0.023	1^a	3.6	Weak	—	Strong	—	—
TG 3	56.1	0.023	1^a	1.9	Not measured by XRD				
TG 4	71.6	0.023	0.2^a	1.3	Not measured by XRD				
IH 1	38	0.043	3	—	Weak	—	Strong	—	—
IH 2	37	0.030	3	—	—	—	Strong	—	—
IH 3	55	0.13	3	—	Strong	Weak	—	—	—
IH 4	56	0.10	4	—	Strong	Weak	—	—	—
IH 5	55	0.088	3	—	—	—	Strong	—	—
IH 6	55	0.079	3	—	—	—	Strong	—	—
IH 7	69	0.24	3	—	Weak	Weak	—	Strong	—
IH 8	69	0.14	3	—	—	—	Strong	—	Weak
IH 9	79	0.40	4	—	Weak	Weak	—	Strong	—
IH 10	79	0.36	3	—	—	Strong	—	Weak	—
IH 11	79	0.32	3	—	—	Strong	—	—	—
IH 12	78	0.18	3	—	—	Weak	Strong	—	Weak
IH 13	78	0.14	3	—	—	—	Strong	—	Weak
IH 14	84	0.44	3	—	—	Strong	—	Weak	—

[a] "Time" for TG measurements represents the time required for a 90% mass increase relative to the final achieved mass at the end of the measurement. [b] x: hydration number. [c] Detected hydrated phases: hydrated phases detected by XRD measurements in the samples after the isothermal TG measurements and the isothermal hydration treatments (No. 1–14). "Strong" and "weak" represent the relative intensity of the XRD peaks derived from each phase. The phase with "strong" corresponds to the main phase formed in the hydration treatments (TG 1–4, IH 1–14) whereas the phase with "weak" corresponds to the secondary phases. [d] Rhombohedral: Rhombohedral $Y_2(SO_4)_3 \cdot xH_2O$

$Y_2(SO_4)_3 \cdot 4H_2O$ is generated as an intermediate phase in the dehydration process of $Y_2(SO_4)_3 \cdot 8H_2O$ to $Y_2(SO_4)_3$.[21] In contrast, our TG curve (Fig. 1) of rhombohedral $Y_2(SO_4)_3$ suggest another hydrate phase $Y_2(SO_4)_3 \cdot H_2O$. Here, we further investigate in detail the high-temperature and the low-temperature dehydration/hydration reactions.

3.1.1 High-temperature dehydration/hydration reaction. The crystal structure changes from $Y_2(SO_4)_3 \cdot xH_2O$ to rhombohedral $Y_2(SO_4)_3$ during the dehydration reaction were investigated by high-temperature XRD. Fig. 2 shows XRD patterns during dehydration upon heating from 50 °C to 150 °C under humidified oxygen ($p_{H_2O} = 0.03$ atm) and the reported diffraction peak positions of rhombohedral $Y_2(SO_4)_3$ (PDF#00-042-0236). Based on TG curves (Fig. 1), the XRD patterns below 110 °C (50, 70, and 90 °C) represent $Y_2(SO_4)_3 \cdot xH_2O$ ($x \geq 1$, depending on temperature), while those at higher temperatures (130 and 150 °C) represent rhombohedral $Y_2(SO_4)_3$. The marks shown above each XRD pattern except one at 110 °C represent the simulated XRD peaks based on the crystal structure of rhombohedral $Y_2(SO_4)_3$ with modified lattice parameters (a axial length, α angle) derived by Rietveld refinement. As can be seen in Fig. 2, the simulated and measured XRD peaks agree well at every temperature. Since the XRD patterns at each temperature are interpreted as rhombohedral $Y_2(SO_4)_3$ structure with the changed lattice parameters, the hydration reaction of rhombohedral $Y_2(SO_4)_3$ should proceed by water insertion into the host lattice. In particular, the overlapping patterns of the $Y_2(SO_4)_3 \cdot xH_2O$ and rhombohedral $Y_2(SO_4)_3$ observed only at

110 °C, represented by the co-existing of "peak a" and "peak b" derived from the hydrate and anhydrate phases respectively. This should account for the steep high-temperature dehydration reaction of $Y_2(SO_4)_3 \cdot xH_2O$ to rhombohedral $Y_2(SO_4)_3$.

Hereinafter we refer to the low-temperature hydrate phase below 110 °C as "rhombohedral $Y_2(SO_4)_3 \cdot xH_2O$ ($x \geq 1$)" and the reaction formula of the high-temperature reaction is written as follows:

$$\text{Rhombohedral } Y_2(SO_4)_3 \text{ (s)} + H_2O \text{ (g)} \rightleftarrows \text{Rhombohedral } Y_2(SO_4)_3 \cdot H_2O \text{ (s)}$$
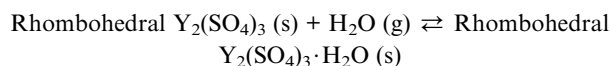
At the lower temperatures (between 50–90 °C), the XRD patterns do not exhibit marked changes, but the hydration number x changes with temperature (see Fig. 1), suggesting that rhombohedral $Y_2(SO_4)_3 \cdot xH_2O$ ($x \geq 1$) has a nonstoichiometric hydration number.

3.1.2 Low-temperature dehydration/hydration reaction. To elucidate the phase changes and the reaction behaviors in the low-temperature hydration reaction, we conducted isothermal TG measurements and isothermal hydration treatments (IH). Table 1 shows the hydration conditions, formed phases, and the largest hydration numbers reached in each isothermal TG measurement and isothermal hydration treatment (IH No. 1–14). Fig. 3 shows the isothermal TG curves obtained by the above measurements. Fig. 4 and 5 show the XRD patterns of the samples after the isothermal TG measurements and isothermal hydration treatments. The results in Fig. 3, 4 and 5 are summarized in Table 1.
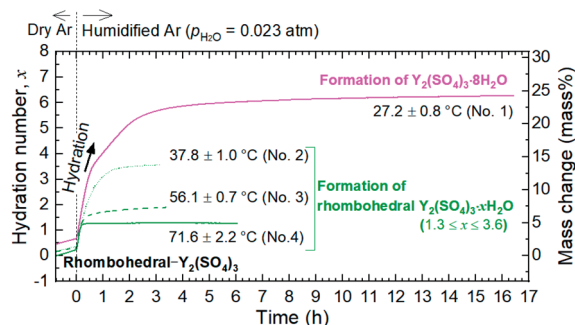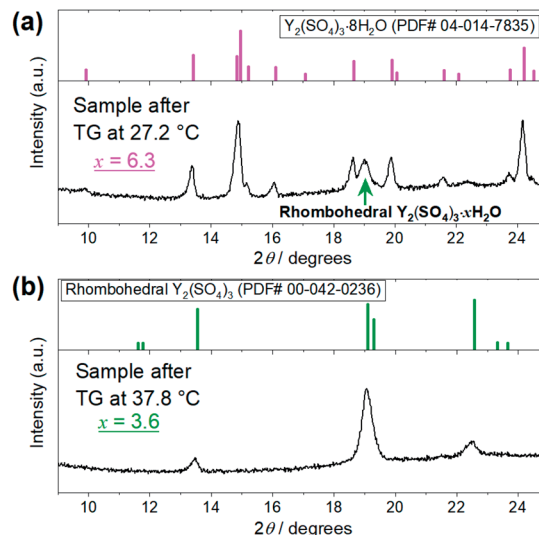
Fig. 3 TG curves of rhombohedral $Y_2(SO_4)_3$ of the isothermal hydration reaction at four different temperatures: 27.2 °C (No. 1), 37.8 °C (No. 2), 56.1 °C (No. 3), and 71.6 °C (No. 4). Temperature during the measurements fluctuated up to 2.2 °C. For these measurements, $Y_2(SO_4)_3 \cdot 8H_2O$ was used as the starting material. It was dehydrated to rhombohedral $Y_2(SO_4)_3$ at 320 °C in TG under dry argon. Then it was cooled to a predetermined temperature. The sample mass of rhombohedral $Y_2(SO_4)_3$ at around 320 °C, used for the basis of mass change, are as follows: 14.17 mg (No. 1), 14.34 mg (No. 2), 13.75 mg (No. 3), 13.54 mg (No. 4). While maintaining a constant temperature, the isothermal hydration reaction started by switching the flowing gas from dry argon to humidified argon ($p_{H_2O} = 0.023$ atm) to examine the hydration process. Horizontal axis shows the elapsed time since the initiation of the hydration reaction by switching the flowing gas from dry argon to humidified argon.

Fig. 4 XRD patterns of the $Y_2(SO_4)_3 \cdot nH_2O$ samples after the TG measurements at (a) 27.2 °C and (b) 37.8 °C shown in Fig. 3. (a) Top figure represents the reference pattern of $Y_2(SO_4)_3 \cdot 8H_2O$ (ICDD (PDF#04-014-7835)). In the bottom figure, there is an XRD peak attributed to the residual rhombohedral $Y_2(SO_4)_3 \cdot xH_2O$ around 19°. (b) Top figure represents the reference pattern of rhombohedral $Y_2(SO_4)_3$ (ICDD (PDF#00-042-0236)).

Depending on the hydration conditions, one or more of three known phases $Y_2(SO_4)_3 \cdot 8H_2O$ (monoclinic), $Y_2(SO_4)_3 \cdot 3H_2O$ (orthorhombic),[25,¶] and rhombohedral $Y_2(SO_4)_3 \cdot xH_2O$ as well as two unknown phases ("Unknown A" and "Unknown B") are present. Based on the isothermal TG results in Fig. 3, rhombohedral $Y_2(SO_4)_3 \cdot H_2O$, which is formed by the high-temperature hydration reaction, further is hydrated to rhombohedral $Y_2(SO_4)_3 \cdot xH_2O$ ($x > 1$) and becomes $Y_2(SO_4)_3 \cdot 8H_2O$ (monoclinic) at lower temperatures. Isothermal hydration treatments under relatively high p_{H_2O} (>0.08 atm) reveal that another intermediate hydrate $Y_2(SO_4)_3 \cdot 3H_2O$ appears at intermediate temperature.

The isothermal TG measurements indicate that rhombohedral $Y_2(SO_4)_3 \cdot xH_2O$ has a nonstoichiometric hydration number x (>1). Fig. 3 shows the isothermal TG curves (TG No. 1–4) in the hydration reaction of rhombohedral $Y_2(SO_4)_3$ at a constant temperature of 27.2 (No. 1), 37.8 (No. 2), 56.1 (No. 3), and 71.6 °C (No. 4) under 0.023 atm of p_{H_2O}. The apparent increase in the hydration number x becomes larger as the holding temperature is lowered: $x = 1.3$ (at 71.6 °C), 1.9 (at 56.1 °C), 3.6 (at 37.8 °C), and 6.3 (at 27.2 °C). Fig. 4(a) and (b) show the XRD patterns of the samples after the isothermal TG measurements at 27.2 °C and 37.8 °C. The pattern of the 6.3 hydrate-equivalent sample confirms the partial formation of $Y_2(SO_4)_3 \cdot 8H_2O$ (monoclinic), while the pattern of the 3.6 hydrate-equivalent sample indicates a single-phasic pattern quite similar to that of rhombohedral $Y_2(SO_4)_3 \cdot xH_2O$ shown in Fig. 2. Therefore,

rhombohedral $Y_2(SO_4)_3 \cdot xH_2O$ may have a nonstoichiometric hydration number x and accommodate water molecules form $x = 1$ to at least $x = 3.6$. Such non-stoichiometry of hydrates has also been reported for $MgSO_4 - H_2O$ system.[4]

In the 6.3 hydrate-equivalent sample, the rhombohedral $Y_2(SO_4)_3 \cdot xH_2O$ phase still remains even after the isothermal TG curve (No. 1) reaches a plateau. This suggests that the hydration reaction of rhombohedral $Y_2(SO_4)_3 \cdot xH_2O$ to $Y_2(SO_4)_3 \cdot 8H_2O$ was significantly slowed down in the middle of the reaction but the cause is unclear at this time. Based on Gibbs' phase rule, the equilibrium solid phase in the hydration reaction should be a single-phase. Thus $Y_2(SO_4)_3 \cdot 8H_2O$ is regarded as the equilibrium phase in the conditions (27.2 °C, $p_{H_2O} = 0.023$ atm).‖

According to the isothermal TG curves, the hydration reactions are almost complete in 3 hours. Therefore, it is reasonable that the equilibrium phases are contained in the detected phases in each batch (No. 1–14) and we can assume that the phase with the largest hydration number is the equilibrium hydrate for each condition. Based on this assumption, we constructed the phase stability diagram of $Y_2(SO_4)_3$ hydrates with temperature and water vapor pressure (T–p_{H_2O} map) shown in Fig. 6. Only $Y_2(SO_4)_3 \cdot 8H_2O$ (monoclinic), $Y_2(SO_4)_3 \cdot 3H_2O$

¶ The crystal structure of $Y_2(SO_4)_3 \cdot 3H_2O$ is considered to be the same as that of $Yb_2(SO_4)_3 \cdot 3H_2O$ reported by Mills *et al.*[25] The XRD pattern of $Y_2(SO_4)_3 \cdot 3H_2O$ shown in Fig. 5 as orange inverted triangles was estimated by adjusting only the diffraction angles of XRD peaks of $Yb_2(SO_4)_3 \cdot 3H_2O$ while the peak intensities were left as is.

‖ Focusing only on condensed phases in the $Y_2(SO_4)_3$–H_2O pseudo-binary system, the degree of freedom F is represented as follows: $F = C - P + 2 = 4 - P$, where C is the number of independent components and P is the number of condensed phases. In the case of the isothermal hydration reaction of $Y_2(SO_4)_3$, the temperature and the total pressure are fixed and the chemical potential of H_2O is determined by the water vapor pressure of gas phase equilibrated with the $Y_2(SO_4)_3$–H_2O system. Then the degree of freedom becomes $F = 1 - P$. Because the F should be larger than zero, the number of the solid phase should be 1 at most.
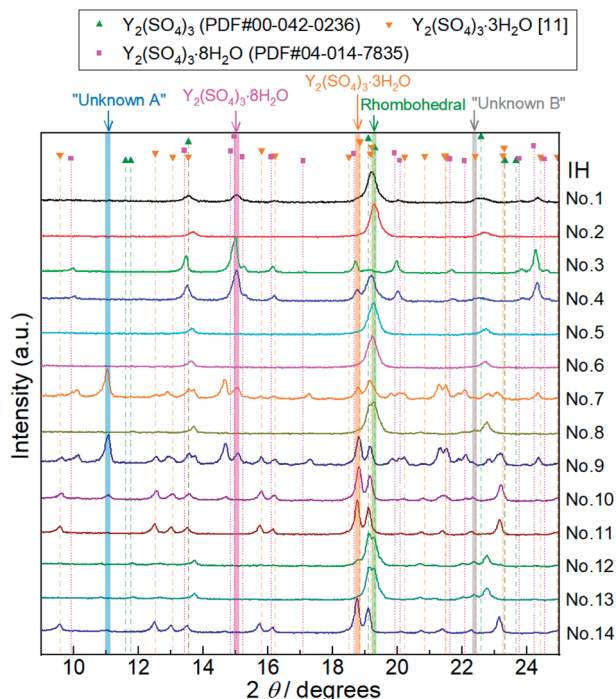
Fig. 5 XRD patterns of $Y_2(SO_4)_3$ hydrate samples after 14 batches of isothermal hydration treatments (IH No. 1–14). Characteristic diffraction angles where distinctive peaks of $Y_2(SO_4)_3 \cdot 8H_2O$, $Y_2(SO_4)_3 \cdot 3H_2O$,[25] rhombohedral $Y_2(SO_4)_3 \cdot xH_2O$ (Rhombohedral), Unknown A, and Unknown B exist are highlighted by pink, orange, green, blue, and gray, respectively. Peaks at 11.1° highlighted by a blue belt (No. 7, 9, 10, and 14) do not match any of the reported reference pattern peaks. These peaks are attributed to an unknown hydrated phase Unknown A. Similarly, we assumed that the peak at 22.4° highlighted by gray (No. 8, 12, and 13) is attributed to Unknown B. Doublet peaks around 19° are also attributed to Unknown B.

(orthorhombic), and rhombohedral $Y_2(SO_4)_3 \cdot xH_2O$ are considered.

Both Unknown A and Unknown B are not considered in constructing the T–p_{H_2O} map for the following reasons. Unknown A and Unknown B are some hydrate phases of $Y_2(SO_4)_3$. Based on the detected conditions for them, the estimated hydration number of Unknown A is between 3 to 8 and that of Unknown B is between 1 to 3. Unknown A and Unknown B might have stable T–p_{H_2O} regions near the broken lines B and C respectively but the regions should not be wide because they are always accompanied by rhombohedral $Y_2(SO_4)_3 \cdot xH_2O$, $Y_2(SO_4)_3 \cdot 3H_2O$, or $Y_2(SO_4)_3 \cdot 8H_2O$ (see Table 1). As Unknown A and Unknown B are intermediate hydrate phases between the considered phases, even though they are omitted in Fig. 6, it should be sufficient to know the outline of the relationship between the hydration conditions and hydration number changes.

3.2 Microstructures of rhombohedral $Y_2(SO_4)_3$

The microstructures of rhombohedral $Y_2(SO_4)_3$ obtained by dehydration of $Y_2(SO_4)_3 \cdot 8H_2O$ were investigated. Fig. 7(a) shows the N_2 adsorption isotherms of $Y_2(SO_4)_3 \cdot 8H_2O$ and rhombohedral $Y_2(SO_4)_3$. The specific surface area of rhombohedral $Y_2(SO_4)_3$ by the BET method (7 m² g⁻¹) is more than

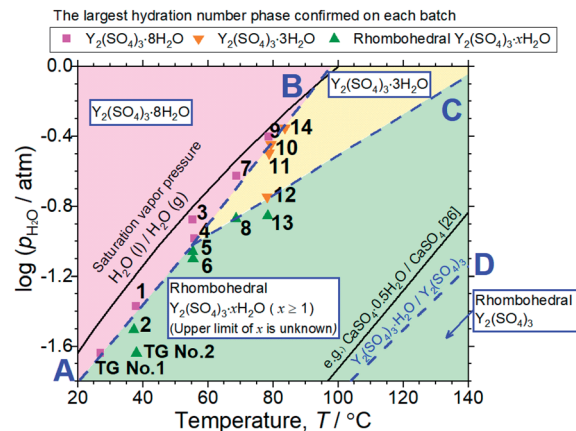**Fig. 6** T–p_{H_2O} map derived from 14 batches of hydration treatments that expose rhombohedral $Y_2(SO_4)_3$ under various temperatures and p_{H_2O} for 3 hours. Here, only batches No. 4 and 9 are held for 4 hours. Additionally, the results of the isothermal TG measurements (Fig. 3) and the XRD (Fig. 4) are also represented by "TG No. 1" and "TG No. 2". Pink squares represent batches where $Y_2(SO_4)_3 \cdot 8H_2O$ is formed. Orange inverted triangles represent batches where $Y_2(SO_4)_3 \cdot 3H_2O$ is formed but $Y_2(SO_4)_3 \cdot 8H_2O$ is not. Green triangles represent batches where neither $Y_2(SO_4)_3 \cdot 3H_2O$ and $Y_2(SO_4)_3 \cdot 8H_2O$ are formed. Two-phase equilibria are represented by broken lines. Broken lines A and B show the minimum p_{H_2O} and maximum temperature required to form $Y_2(SO_4)_3 \cdot 8H_2O$. Broken line C also shows those required to form $Y_2(SO_4)_3 \cdot 3H_2O$. Broken line D represents the equilibrium between rhombohedral $Y_2(SO_4)_3$ and rhombohedral $Y_2(SO_4)_3 \cdot H_2O$. It is drawn using the estimated enthalpy and entropy changes of the dehydration/hydration reaction, determined by TG measurements under four different p_{H_2O}. See ESI-2† for the TG curves. Temperature dependences of the saturation vapor pressure of liquid water and the equilibrium between $CaSO_4$ and $CaSO_4 \cdot 0.5H_2O$ are also shown.[26]

a hundredfold larger than that of the $Y_2(SO_4)_3 \cdot 8H_2O$ (0.05 m² g⁻¹). ESI-3† shows the BET plots. Fig. 8 shows photographs of (a) $Y_2(SO_4)_3 \cdot 8H_2O$ and (b) rhombohedral $Y_2(SO_4)_3 \cdot xH_2O$ particles observed by optical microscopy. Note that the hydration number x of the rhombohedral phase was not known unclear accurately because rhombohedral $Y_2(SO_4)_3$ hydrates to some extent in air. $Y_2(SO_4)_3 \cdot 8H_2O$ particles show facet planes and high transparency, and they are likely a-few-hundreds-µm-large single crystals. On the other hand, rhombohedral $Y_2(SO_4)_3 \cdot xH_2O$ particles are less transparent representing the polycrystalline nature. Correspondingly, a dark-field TEM image of rhombohedral $Y_2(SO_4)_3$ in Fig. 9 reveals crevices and voids at a-few-micrometer intervals.** A similar microstructure formation is observed in the case of dehydration of $La_2(SO_4)_3 \cdot 9H_2O$ to β-$La_2(SO_4)_3$ (Fig. 7(b)), which is known to improve the kinetics of hydration/dehydration reaction of β-$La_2(SO_4)_3$.[17] The microstructure of rhombohedral $Y_2(SO_4)_3$ is also expected to promote the hydration/dehydration reaction rates by extending the surface area and shortening the diffusion length of water in the crystals although it was not confirmed yet.

** We did not conduct TEM observations on $Y_2(SO_4)_3 \cdot 8H_2O$ due to the difficulty with sample preparation. The dehydration reaction of $Y_2(SO_4)_3 \cdot 8H_2O$ proceeded even under a vacuum at room temperature on FIB processing for sample preparation.
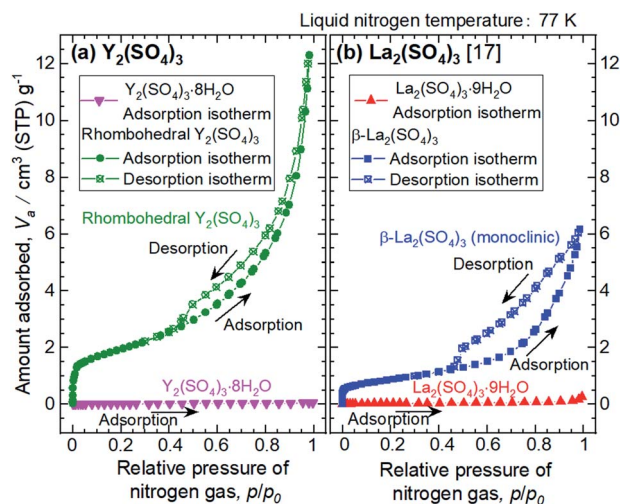
Fig. 7 Adsorption/desorption isotherms obtained by N_2 adsorption measurements on (a) $Y_2(SO_4)_3$ and (b) $La_2(SO_4)_3$ for comparison. Pink inverted triangles show the isotherms of $Y_2(SO_4)_3 \cdot 8H_2O$. Green circles denote the isotherms of rhombohedral $Y_2(SO_4)_3$ prepared by heating $Y_2(SO_4)_3 \cdot 8H_2O$ at 200 °C for 1 hour in air. Both samples are measured after a vacuum pretreatment for 1000 minutes at room temperature. Phase of both samples unchanged after N_2 adsorption measurements, which is confirmed by XRD. Vertical axis represents V_a, which means the volume of adsorbed nitrogen gas under standard temperature and pressure (STP). Here, the temperature is 273.15 K and the gas pressure is 101.325 kPa. Horizontal axis shows the relative pressure p/p_0 where p is the equilibrium pressure and p_0 is the saturation nitrogen gas pressure over liquid nitrogen at 77 K.
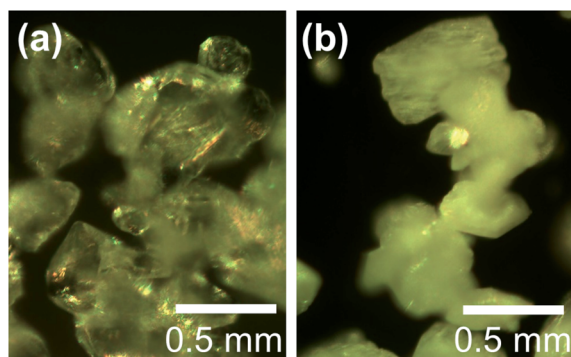

Fig. 8 Optical microscope images of (a) $Y_2(SO_4)_3 \cdot 8H_2O$ and (b) rhombohedral $Y_2(SO_4)_3 \cdot xH_2O$ particles. Rhombohedral $Y_2(SO_4)_3$ made from $Y_2(SO_4)_3 \cdot 8H_2O$ by heating at 270 °C for 2 hour in air. Both particles look yellowish due to the light source of the optical microscope. Actually, $Y_2(SO_4)_3 \cdot 8H_2O$ is colorless and rhombohedral $Y_2(SO_4)_3$ is white under white light.

4. Discussion

4.1 Relationships between water insertion mechanisms and reaction temperature ranges: comparison of rhombohedral $Y_2(SO_4)_3$ and β-$La_2(SO_4)_3$

The high-temperature hydration reaction of rhombohedral $Y_2(SO_4)_3 \cdot xH_2O$ ($x = 0$ or ~1) likely proceeds by water insertion into the crystal lattice (see Section 3.1.1). This reaction is similar
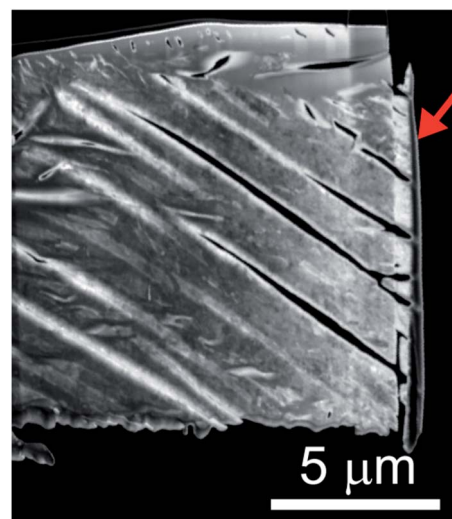

Fig. 9 Dark-field TEM image of the rhombohedral $Y_2(SO_4)_3$ specimen cut out from the rhombohedral $Y_2(SO_4)_3$ particle by FIB processing. Rhombohedral $Y_2(SO_4)_3$ made from $Y_2(SO_4)_3 \cdot 8H_2O$ by heating at 200 °C for 1 hour in air. Vertical black few-hundred-nm-thick layer at the right edge of the sample indicated by the red arrow is deposited carbon for FIB processing following the same procedure used in ref. 17.

to the hydration reaction of β-$La_2(SO_4)_3 \cdot xH_2O$ ($0 \leq x \leq 1$) (monoclinic).[15] However, their water insertion mechanisms differ. Regarding β-$La_2(SO_4)_3 \cdot xH_2O$, the hydration number x changes continuously with maintaining a single-phase nature during the dehydration/hydration reactions. In contrast, the high-temperature hydration reaction of rhombohedral $Y_2(SO_4)_3$ is a "two-phase reaction" because two different phases (rhombohedral $Y_2(SO_4)_3$ and rhombohedral $Y_2(SO_4)_3 \cdot H_2O$) co-exist during the dehydration at 110 °C (see Section 3.1.1 and Fig. 2). Fig. 10 schematically depicts the dehydration processes of (a) the two-phase reaction and (b) the "single-phase reaction". The two-phase reaction proceeds as the ratio of hydrated and dehydrated phases changes, while the single-phase reaction proceeds as the hydration number of the single solid phase continuously decreases. A two-phase reaction proceeds at a single equilibrium temperature in principle. Thus, the two-phase reaction with a sufficiently fast reaction rate can complete reversible reactions in a narrow temperature range (*e.g.*, rhombohedral $Y_2(SO_4)_3 \cdot xH_2O$ ($x = 0 \rightleftarrows$ ~1): 80–130 °C at a rate of 1 °C min^{-1}). On the other hand, a single-phase reaction advances with changing the hydration number and the equilibrium temperature continuously in principle. Even if the reaction rate is fast enough, the reaction temperature range broadens (*e.g.*, β-$La_2(SO_4)_3 \cdot xH_2O$: 80–250 °C at a rate of 1 °C min^{-1} (ref. 15)). Therefore, the two-phase reaction with a sufficiently fast reaction rate is preferred for the TCHS system as the required temperature range for reaction completion narrows.

4.2 Applicability of rhombohedral $Y_2(SO_4)_3$ as a TCHS material

Based on the T–p_{H_2O} map (Fig. 6), we consider an application of several reactions of rhombohedral $Y_2(SO_4)_3$ to chemical heat
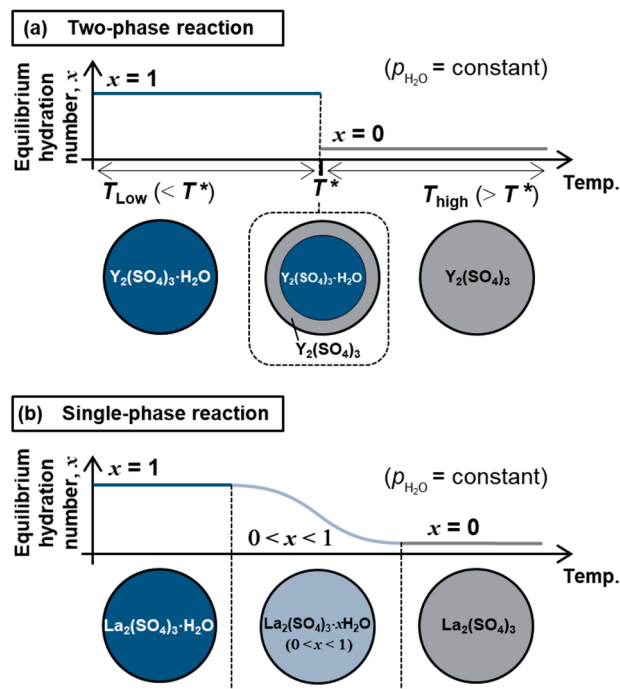
Fig. 10 Schematic diagrams of the dehydration processes for (a) the two-phase reaction of rhombohedral $Y_2(SO_4)_3$ and (b) the single-phase reaction of β-$La_2(SO_4)_3$. (a) Top figure is the schematic graph showing the change of equilibrium hydration number x with temperature increase. Here, T^* represents the equilibrium temperature of the two-phase reaction between rhombohedral $Y_2(SO_4)_3$ and rhombohedral $Y_2(SO_4)_3 \cdot H_2O$. The schematic diagram under the graph shows the schematic of hydration number distribution of rhombohedral $Y_2(SO_4)_3 \cdot H_2O$ spherical particle during heating. When the temperature is below T^*, the equilibrium phase is rhombohedral $Y_2(SO_4)_3 \cdot H_2O$. At the equilibrium temperature T^*, both phases are co-existing until the dehydration reaction finishes. Then rhombohedral $Y_2(SO_4)_3$ is the equilibrium phase when the temperature is upon T^*. (b) The schematic graph showing the continuous change of equilibrium hydration number of β-$La_2(SO_4)_3 \cdot xH_2O$ with temperature increase. The schematic diagram under the graph shows the schematic of hydration number distribution of β-$La_2(SO_4)_3 \cdot xH_2O$ spherical particle during the dehydration reaction based on the single-phase reaction.

pumps to upgrade thermal energy. The application employs an apparatus consisting of a reactor containing rhombohedral $Y_2(SO_4)_3$ and an evaporator containing water. In the heat releasing step, saturated water vapor is transported from the evaporator to the reactor and rhombohedral $Y_2(SO_4)_3$ is hydrated. Here, the temperature lift (the temperature difference between the evaporator and the reactor) should ideally be equal to the difference between the dew point of water and the equilibrium temperature of the hydration reaction at a constant p_{H_2O}. The equilibrium temperatures, the temperature lifts attained by reactions A, B, C, and D shown in Fig. 6 are represented by the temperature differences between the saturation vapor pressure line and the broken lines A, B, C, and D at a constant p_{H_2O} (Fig. 6). As can be seen, reaction D (high-temperature reaction: $Y_2(SO_4)_3/Y_2(SO_4)_3 \cdot H_2O$) works similarly to the hydration reaction of $CaSO_4$ in terms of the temperature lift. Reaction C ($Y_2(SO_4)_3 \cdot xH_2O/Y_2(SO_4)_3 \cdot 3H_2O$) may also be

utilized under high p_{H_2O} (> ~0.08 atm). On the other hand, using the two-step reaction of C and D is disadvantageous in that they output heat at different temperatures which leads to a large temperature drop against stored heat. The reactions A ($Y_2(SO_4)_3 \cdot xH_2O/Y_2(SO_4)_3 \cdot 8H_2O$) and B ($Y_2(SO_4)_3 \cdot 3H_2O/Y_2(SO_4)_3 \cdot 8H_2O$) may not be suitable for practical applications due to the small temperature lift (approximately 10 °C).

We also discuss in terms of heat storage density. The standard enthalpy change of the high-temperature dehydration reaction of rhombohedral $Y_2(SO_4)_3 \cdot H_2O$ (reaction D) was estimated by a van't Hoff plot. The relationship between p_{H_2O} and the equilibrium temperature of the reaction was assessed by TG measurements on rhombohedral $Y_2(SO_4)_3 \cdot H_2O$ under four different p_{H_2O} (ESI-2†). Fig. 11 shows the van't Hoff plot constructed from the equilibrium temperatures and p_{H_2O}. From the slope of the approximated straight line, the estimated standard enthalpy change $\Delta H°$ of rhombohedral $Y_2(SO_4)_3 \cdot H_2O$ is 46 kJ $(\text{mol-}H_2O)^{-1}$ or 99 kJ $(\text{kg-hydrate})^{-1}$. The small gravimetric standard enthalpy change is attributed to the small hydration water content, *i.e.* the mass change with reaction D, equal to 3.72 mass%.

However, if the additional hydration reaction C with 10.3 mass% of mass change is utilized, a larger heat storage capacity is expected although the $\Delta H°/\text{kJ (kg-hydrate)}^{-1}$ of $Y_2(SO_4)_3 \cdot 3H_2O$ is not measured. Note that, among the dehydration/hydration reaction systems having similar equilibrium temperatures, the magnitude of $\Delta H°/\text{kJ (kg-hydrate)}^{-1}$ dominantly depends on the mass change. This is because the $\Delta H°/\text{kJ (mol-}H_2O)^{-1}$ of dehydration reaction is approximately proportional to the equilibrium temperature.[27] See (ESI-4)† for the relationship between the $\Delta H°$ and the equilibrium temperature. Thus, the mass change with the dehydration/hydration reaction is an indicator to simply evaluate the magnitude of the $\Delta H°/\text{kJ (kg-hydrate)}^{-1}$.

Here, the gravimetric energy densities of $Y_2(SO_4)_3 \cdot 3H_2O$ and $Y_2(SO_4)_3 \cdot H_2O$ are compared with other materials. The $\Delta H°$ or mass change of $Y_2(SO_4)_3 \cdot 3H_2O$ (10.4 mass%) and $Y_2(SO_4)_3 \cdot H_2O$ (99 kJ $(\text{kg-hydrate})^{-1}$, 3.72 mass%) is significantly lower than other salt hydrates with larger hydration numbers or with lower mass, for example, $MgSO_4 \cdot 6H_2O$ (1395 kJ $(\text{kg-hydrate})^{-1}$, 47.3 mass%),[5] $CaCl_2 \cdot 6H_2O$ (1649 kJ $(\text{kg-hydrate})^{-1}$, 49.3 mass%),[28] $Na_2S \cdot 5H_2O$ (1784 kJ $(\text{kg-hydrate})^{-1}$, 53.6 mass%),[11] and $LiOH \cdot H_2O$ (1440 kJ $(\text{kg-hydrate})^{-1}$, 42.9 mass%).[20] Compared with these salt hydrates, an advantage of $Y_2(SO_4)_3$ system is the ease of handling since neither of aggregation due to the melting or deliquescence or skin formation covering the bulk particles has been confirmed in the hydration/dehydration reaction process. Therefore, $Y_2(SO_4)_3$ system may be available for TCHS usage without developing composite materials with porous matrix and, in this respect, similar to $CaSO_4 \cdot 0.5H_2O$ and β-$La_2(SO_4)_3 \cdot H_2O$. The values of $\Delta H°$ and the mass change of $Y_2(SO_4)_3 \cdot 3H_2O$ or $Y_2(SO_4)_3 \cdot H_2O$ are comparable to those of $CaSO_4 \cdot 0.5H_2O$ (240 kJ $(\text{kg-hydrate})^{-1}$ (ref. 26) and 6.21 mass%) and those of β-$La_2(SO_4)_3 \cdot H_2O$ (156 kJ $(\text{kg-hydrate})^{-1}$ (ref. 15) and 3.08 mass%).

For TCHS application, heat output rate is also important but the performance of rhombohedral $Y_2(SO_4)_3$ has never been

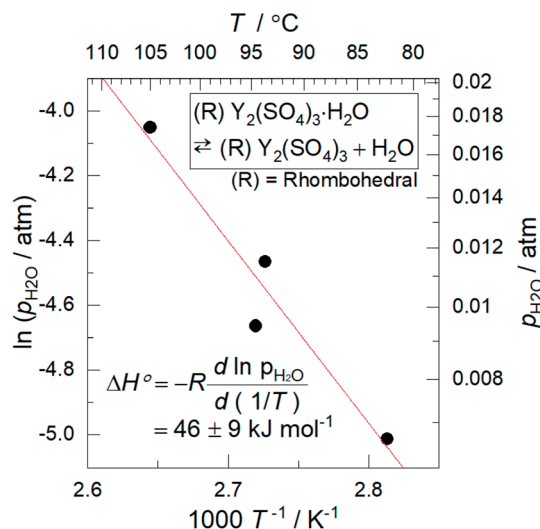Fig. 11 Van't Hoff plot for the high-temperature reaction of rhombohedral $Y_2(SO_4)_3 \cdot H_2O$. The equilibrium temperatures T are the estimated values from the TG measurements under four different p_{H_2O} (ESI-2†). Because rhombohedral $Y_2(SO_4)_3 \cdot H_2O$ dehydrates/hydrates *via* a two-phase reaction, the equilibrium temperature of the reaction (high-temperature reaction) should be a single temperature at each p_{H_2O}.

evaluated yet. Regarding the hydration reaction rate shown in Fig. 3, the hydration reaction with hydration number change x of 1–3 completed within tens of minutes and that with $x = \sim 6$ completed within 3 hours. These hydration reaction rates are comparable to those reported in the hydration of other salts, *i.e.* $MgSO_4$,[5] Na_2S,[11] β-$La_2(SO_4)_3$,[17] and $CaCl_2$.[28]

5. Conclusion

We examine the hydration/dehydration of rhombohedral $Y_2(SO_4)_3$ and their potential as a TCHS material by cyclic TG, high-temperature XRD, isothermal TG, isothermal hydration treatments, nitrogen gas adsorption, optical microscope observations, and TEM observations. TG measurements revealed that rhombohedral $Y_2(SO_4)_3$ can hydrate/dehydrate reversibly below 130 °C with relatively small thermal hysteresis (less than 50 °C) and large change in hydration water content (above 10 mass%). Rhombohedral $Y_2(SO_4)_3$ was found to be a favorable material in terms of the reaction temperature and the reaction behavior. The hydration reaction of rhombohedral $Y_2(SO_4)_3$ proceeds *via* at least two steps: the high-temperature reaction at 80–130 °C and the low-temperature reaction at 30–100 °C in 0.02 atm of p_{H_2O}. The high-temperature hydration reaction proceeds by water insertion into rhombohedral $Y_2(SO_4)_3$ to form rhombohedral $Y_2(SO_4)_3 \cdot H_2O$ with only minor changes in the host crystal structure. In the low-temperature hydration reaction, rhombohedral $Y_2(SO_4)_3 \cdot H_2O$ further hydrates to rhombohedral $Y_2(SO_4)_3 \cdot xH_2O$ ($x > 1$) while maintaining the host structure. There is a possibility that rhombohedral $Y_2(SO_4)_3 \cdot xH_2O$ has a non-stoichiometric hydration number x. At lower temperature (at most 27 °C in 0.02 atm of p_{H_2O}), it finally hydrates to

$Y_2(SO_4)_3 \cdot 8H_2O$ which has a different crystal structure. Furthermore, another intermediate hydrate $Y_2(SO_4)_3 \cdot 3H_2O$ is formed in the hydration reaction under relatively high p_{H_2O} (>0.08 atm) and intermediate temperature.

Regarding the application of rhombohedral $Y_2(SO_4)_3$ to thermochemical heat pumps for energy upgrades, the hydration of rhombohedral $Y_2(SO_4)_3$ to rhombohedral $Y_2(SO_4)_3 \cdot H_2O$ can be used in the same manner as an existing candidate material $CaSO_4 \cdot 0.5H_2O$ in terms of reaction temperature and p_{H_2O}. However, the standard enthalpy change $\Delta H°$ of the dehydration of rhombohedral $Y_2(SO_4)_3 \cdot H_2O$ (46 kJ mol^{-1}) is not sufficient. The hydration of rhombohedral $Y_2(SO_4)_3 \cdot xH_2O$ to $Y_2(SO_4)_3 \cdot 3H_2O$ (hydration water content: 11.6 mass% anhydrous basis) or $Y_2(SO_4)_3 \cdot 8H_2O$ (hydration water content: 30.9 mass% anhydrous basis) enables a larger change in the hydration number and thereby heat storage density, which is characteristic of this reaction system. Concerning the magnitude of the temperature lift on the practical use, the hydration to form $Y_2(SO_4)_3 \cdot 3H_2O$ may be available but that to form $Y_2(SO_4)_3 \cdot 8H_2O$ is not suitable since the temperature lift is as small as approximately 10 °C.

Finally, microstructure formed during the dehydration reaction from $Y_2(SO_4)_3 \cdot 8H_2O$ to rhombohedral $Y_2(SO_4)_3$ was investigated. The estimated surface area of rhombohedral $Y_2(SO_4)_3$ is 7 m^2 g^{-1} while that of the original $Y_2(SO_4)_3 \cdot 8H_2O$ is significantly smaller (0.05 m^2 g^{-1}). Correspondingly, rhombohedral $Y_2(SO_4)_3$ has a fine microstructure with crevices and voids at intervals of a-few-micrometers. Such a fine microstructure is formed by initial dehydration reaction from $Y_2(SO_4)_3 \cdot 8H_2O$ and expected to enhance the dehydration/hydration reaction rates. If the microstructure size can be further improved in the synthesis of rhombohedral $Y_2(SO_4)_3$, a much faster hydration rate is expected.

Conflicts of interest

There are no conflicts to declare.

Acknowledgements

Notes and references

1 P. Pardo, A. Deydier, Z. Anxionnaz-Minvielle, S. Rougé, M. Cabassud and P. Cognet, *Renewable Sustainable Energy Rev.*, 2014, **32**, 591–610.

2 T. Yan, R. Z. Wang, T. X. Li, L. W. Wang and I. T. Fred, *Renewable Sustainable Energy Rev.*, 2015, **43**, 13–31.

3 L. André, S. Abanades and G. Flamant, *Renewable Sustainable Energy Rev.*, 2016, **64**, 703–715.

4 L. Okhrimenko, L. Favergeon, K. Johannes, F. Kuznik and M. Pijolat, *Thermochim. Acta*, 2017, **656**, 135–143.

5 V. Essen, H. Zondag, J. Gores, L. Bleijendaal, M. Bakker, R. Schuitema, W. Helden, Z. He and C. Rindt, *J. Sol. Energy Eng.*, 2009, **131**, 041014.

6 S. Hongois, F. Kuznik, P. Stevens and J.-J. Roux, *Sol. Energy Mater. Sol. Cells*, 2011, **95**, 1831–1837.

7 K. N'Tsoukpoe, H. Rammelberg, A. Lele, K. Korhammer, B. Watts, T. Schmidt and W. Ruck, *Appl. Therm. Eng.*, 2015, **75**, 513–531.

8 M. Kubota, S. Matsumoto, H. Matsuda, H. Huang, Z. He and X. Yang, *Adv. Mater. Res.*, 2014, **953**, 757–760.

9 S. Li, H. Huang, X. Yang, Y. Bai, J. Li, N. Kobayashi and M. Kubota, *Appl. Therm. Eng.*, 2018, **128**, 706–711.

10 M. Kubota, S. Matsumoto and H. Matsuda, *Appl. Therm. Eng.*, 2019, **150**, 858–863.

11 R. Boer, W. Haije and J. Veldhuis, *Thermochim. Acta*, 2003, **395**, 3–19.

12 A. Jong, F. Trausel, C. Finck, L. Vliet and R. Cuypers, *Energy Procedia*, 2014, **48**, 309–319.

13 J.-H. Lee, H. Ogura and S. Sato, *Appl. Therm. Eng.*, 2014, **63**, 192–199.

14 Y. Shiren, M. Masuzawa and N. Kobayashi, *WASET. International Journal of Environmental, Chemical, Ecological, Geological and Geophysical Engineering*, 2015, vol. 9, pp. 803–807.

15 N. Hatada, K. Shizume and T. Uda, *Adv. Mater.*, 2017, **29**, 1606569/1–1606569/6.

16 K. Toyoura, H. Tai, N. Hatada, K. Shizume and T. Uda, *J. Mater. Chem. A*, 2017, **5**, 20188–20194.

17 K. Shizume, N. Hatada, K. Toyoura and T. Uda, *J. Mater. Chem. A*, 2018, **6**, 24956–24964.

18 H. Voigtländer, B. Winkler, W. Depmeier, K. Knorr and L. Ehm, in *Host–Guest Systems Based on Nanoporous Crystals*, ed. F. Laeri, F. Schüth, U. Simon and M. Wark, John Wiley & Sons, New Jersey, 1st edn, 2006, ch. 3, pp. 280–305.

19 R. Perret, B. Rosso and J. Loriers, *Bull. Soc. Chim. Fr.*, 1968, **7**, 2698–2699.

20 M. Kubota, S. Matsumoto and H. Matsuda, *Appl. Therm. Eng.*, 2019, **150**, 858–863.

21 B. Rosso, R. Perret and J. Lories, *C. R. Hebd. Seances Acad. Sci.*, 1968, **267**, 379–382.

22 W. Wendlandt, *J. Inorg. Nucl. Chem.*, 1958, **7**, 51.

23 D. Bernhardt, I. Reilly and J. Mineral, *Commodity Summaries 2019*, Department of the Interior (DOI), U.S. Geological Survey (USGS), Reston, VA, USA, 2019.

24 K. Shizume, N. Hatada, K. Toyoura, H. Tai, S. Yasui and T. Uda, *Presented in part at the IMPRES2019*, Kanazawa, October, 2019.

25 S. Mills, V. Petříčicek, A. R. Kampf, R. Herbst-Imer and M. Raudsepp, *J. Solid State Chem.*, 2011, **184**, 2322–2328.

26 S. Lee, H. Matsuda and M. Hasatani, *Kagaku Kogaku Ronbunshu*, 1986, **12**, 75–82.

27 S. Kiyabu, J. Lowe, A. Ahmed and D. Siegel, *Chem. Mater.*, 2018, **30**, 2006–2017.

28 F. Trausel, A.-J. Jong and R. Cuypers, *Energy Procedia*, 2014, **48**, 447–452.